Maximum entropy deconvolution of resonant inelastic x-ray scattering spectra

J. Laverock, A. R. H. Preston, D. Newby, Jr., K. E. Smith, and S. B. Dugdale

Phys. Rev. B **84**, 235111 — Published 5 December 2011

DOI: 10.1103/PhysRevB.84.235111

Maximum entropy deconvolution of resonant inelastic x-ray scattering spectra

J. Laverock, A. R. H. Preston, D. Newby, Jr., and K. E. Smith
Department of Physics, Boston University, 590 Commonwealth Avenue, Boston, Massachussetts, MA 02215, USA

S. B. Dugdale
H. H. Wills Physics Laboratory, University of Bristol, Tyndall Avenue, Bristol BS8 1TL, United Kingdom

Resonant inelastic x-ray scattering (RIXS) has become a powerful tool in the study of the electronic structure of condensed matter. Although the linewidths of many RIXS features are narrow, the experimental broadening can often hamper the identification of spectral features. Here, we show that the Maximum Entropy technique can successfully be applied in the deconvolution of RIXS spectra, improving the interpretation of the loss features without a severe increase in the noise ratio.

PACS numbers:

I. INTRODUCTION

Over the last decade or so, the technique of resonant inelastic soft x-ray scattering (RIXS) has developed into a formidable tool in the study of the electronic structure of the solid state[1,2], nanomaterials[3], and even liquids and gases[4,5]. The strengths of RIXS using soft x-rays owe to its bulk sensitivity, atomic (and even orbital) selectivity, ability to sample finite momentum transfer and narrow linewidth. Indeed, the recent development of sub-100 meV resolution grating spectrometers[6] has opened up the new possibility of using soft x-rays to study low-energy collective excitations such as magnons or orbitons, and even to track their dispersion in momentum[7,8].

In the RIXS process, a core electron is excited into an unoccupied valence orbital, creating a core hole in the intermediate state which then rapidly (and coherently) decays to the final state via x-ray emission (see, for example, Refs.[1,2]). The incident x-ray is tuned near the threshold of a particular core electron excitation, granting RIXS its site and orbital selectivity. For example, for transition metal L-edges the process is of the form, $2p^6\,3d^n \rightarrow 2p^5\,3d^{n+1} \rightarrow 2p^6\,3d^{n*}$, in which the * denotes an excited state. The final state may be an excited configuration (e.g. dd^* crystal-field transition) or a collective excitation, and the energy difference between the incident and emitted x-rays represents the excitation energy.

Typically however, for soft x-ray RIXS where charge-transfer and/or crystal-field excitations are of interest, the combined energy resolution of the incident photons and RIXS spectrometer amounts to 0.5 – 1.0 eV near the O K-edge ($\sim$ 520 eV). On the other hand, the typical energy of transition metal dd^* crystal field excitations is of the order of 1 – 4 eV, and their separation can be close to the limit of the resolving power of moderate-resolution instruments (for example, low-energy dd^* transitions in VO_2[9,10]). Moreover, even in high-resolution measurements, different low-energy collective excitations can lie in close proximity relative to the resolution function; for example, bi- and single magnon peaks as well as phonon contributions within 400 meV in La_2CuO_4[11]. There is therefore a sensitive trade-off between statistical precision and resolution for these kinds of measurements, which are perfectly poised to take advantage of the benefits of a reliable deconvolution procedure.

The technique of Maximum Entropy (MaxEnt) owes its origins to the study of communication theory introduced by Shannon[12], in which the proposed measure of information content, S, had the same form as the thermodynamic entropy,

$$S = -k \sum_{i,j} p_{i,j} \ln p_{i,j}, \tag{1}$$

in which $p_{i,j}$ is the number of counts in a pixel (i,j) and k is an arbitrary constant. The basic idea of MaxEnt is relatively simple: one maximizes the information content, S, of the processed (deconvoluted) probability distribution subject to it being consistent with the measured data. This consistency test is achieved through a χ^2 comparison between the processed distribution, convoluted with the (known) resolution function, and the measured distribution. The outcome of this process is a distribution that is 'most likely' to have been responsible for the measured data, given the properties of the resolution function.

The algorithm employed here is the Cambridge Algorithm[13] and has been successfully applied to many fields of data analysis, e.g. positron annihilation[14,15], image analysis, astrophysics and extended x-ray absorption fine structure data[16]. The solution of the algorithm is iteratively updated in three 'search directions' $d_{i,j,n}$, with coefficients α_n:

$$p'_{i,j} = p_{i,j} + \sum_{n=1}^{3} \alpha_n d_{i,j,n}. \tag{2}$$

The search directions used in this algorithm are ∇S (to maximize the entropy), $\nabla \chi^2$ (to minimize the χ^2), and a third direction involving higher derivatives. The solution, $p'_{i,j}$, and coefficients α_n are updated at each iteration until convergence in the solution is achieved. The par-

ticular benefit of the MaxEnt procedure over more traditional Fourier transform-based deconvolution methods is the substantially improved signal-to-noise ratio (which will be discussed in more detail in Section V), even when faced with sparse (or missing) data[16].

In the following, all measurements were performed at the AXIS endstation of beamline 7.0.1 of the Advanced Light Source, Lawrence Berkeley National Laboratory, employing a Nordgren-type grating spectrometer[17]. Spectra were recorded on a 2D multi-channel plate detector. Correction for the curvature introduced by the optical components of the spectrometer was achieved by fitting the peak position of several well-characterized sharp emission features across the non-dispersive axis of the detector. This correction was then used for all subsequent spectra. The MaxEnt procedure was applied to the raw 2D spectra before curvature correction. This was found to produce more favorable results compared with processing corrected, integrated 1D spectra, a finding that is expected owing to the greater information content of the 2D images. The MaxEnt deconvolution process involves convolving the processed data with the known resolution function (the 'broadening' function), for which there are two components in RIXS measurements: i) the energy resolution of the incident photons, and ii) the spectrometer resolution. The second of these, predominantly arising from the finite source size, is much more easily dealt with: it is approximately Gaussian with respect to the wavelength of the emitted photons. An accurate knowledge of the incident photon resolution is much more challenging since its impact on emission spectra is non-trivial and depends in part on the specific excitations involved in the vicinity of the incident photon energy (i.e. the absorption spectrum); no attempt has been made to remove this component from the experimental data.

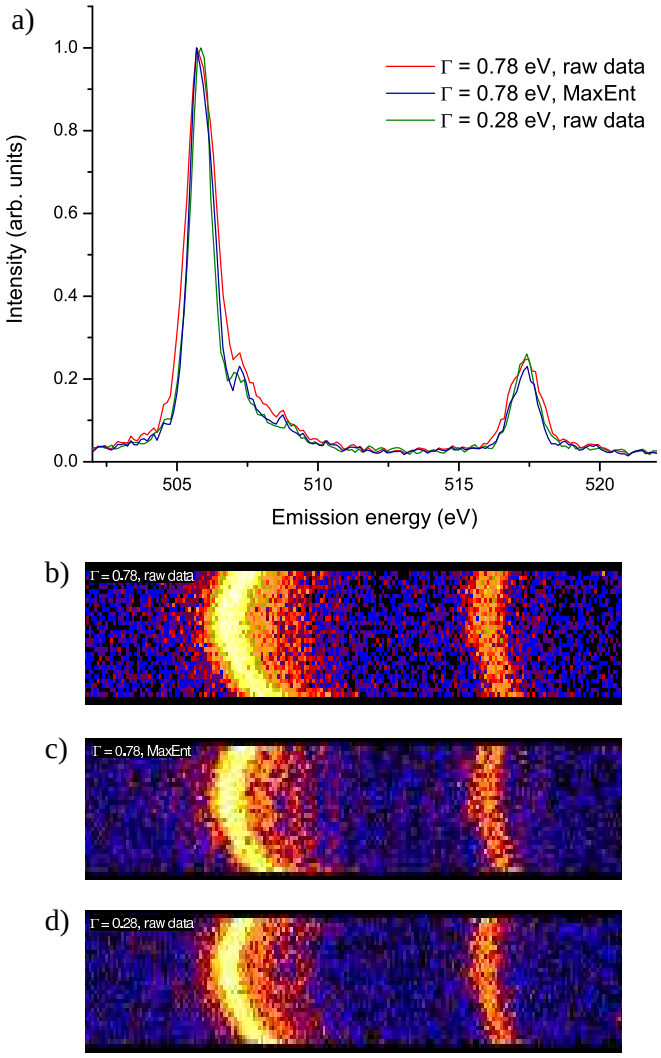

FIG. 1: (Color online) Comparison between raw (second order) Zn x-ray emission spectra recorded at 0.78 eV spectrometer resolution and the results of the MaxEnt deconvolution procedure. For comparison, a spectrum recorded at 0.28 eV spectrometer resolution is also shown. a) Integrated spectra, b) raw 2D spectrum for $\Gamma = 0.78$ eV, c) MaxEnt deconvoluted 2D spectrum for $\Gamma = 0.78$ eV, and d) raw 2D spectrum for $\Gamma = 0.28$ eV. The raw 2D spectra (before correcting for the curvature of the image) are shown on a logarithmic false color scale.

II. DECONVOLUTION OF REFERENCE SPECTRA

As an initial diagnosis of the performance of the MaxEnt procedure, x-ray emission spectra of the $L_{3,2}$-edge of Zn were obtained at various different spectrometer slit widths, corresponding to different spectrometer resolutions. These spectra represent transitions of the form $3d \rightarrow 2p$ with the spin-orbit split L_3 edge at a lower energy than the L_2 emission line. Since we are dealing with emission features, excited well above the absorption threshold, the incident photon energy does not contribute to the overall resolution of these measurements, and they therefore provide a robust test of the MaxEnt procedure in removing the spectrometer part of the resolution function. In Fig. 1, Zn spectra recorded (in second order[18]) with spectrometer resolutions of 0.28 eV and 0.78 eV at FWHM are shown, alongside the results of the MaxEnt deconvolution of the 0.78 eV spectrum. A broadening function of 0.66 eV (85% of the spectrometer resolution) was used in the MaxEnt deconvolution routine. It is clear from Fig. 1 that the width of the deconvoluted spectrum is much narrower than the raw spectrum, and indeed approaches the width of the narrower 0.28 eV spectrum, indicating that a large portion of the instrument resolution has been removed from the spectrum. In fact, this narrowing of the line width of the emission lines is already visible in the raw 2D spectra shown in Fig. 1b-d. The FWHM of the L_3 edge (including the natural width of this feature) is 1.29 eV for the raw spectrum, compared with 1.06 eV after deconvolution. For comparison, the FWHM of the same feature in the narrower raw spectrum

is 1.00 eV. Moreover, there are no additional artefacts introduced in the deconvolution procedure – the MaxEnt spectrum closely resembles the 0.28 eV spectrum. The behavior of the deconvolution with varying broadening functions was also investigated, and found to be very stable for functions of FWHM $\leq$ 90% of the total resolution function. Above this, some artificial sharpening close to the emission peaks was observed. Finally, it is worth noting that the signal-to-noise ratio is not significantly decreased in the deconvoluted spectra (a subject to which we will return in Section V).

III. DECONVOLUTION OF CRYSTAL FIELD EXCITATIONS

In order to test its performance in resolving close spectral features, the MaxEnt deconvolution procedure was applied to Co L-edge RIXS data of $Co_3V_2O_8$, which is a kagomé staircase compound consisting of $Co^{2+}O_6$ octahedra separated by $V^{5+}O_4$ tetrahedra[19]. Spectra were recorded in second order with a spectrometer resolution of 0.82 eV and an incident photon resolution of 0.4 eV, amounting to a total resolution of approximately 0.91 eV. For the MaxEnt deconvolution procedure, a broadening function of 0.82 eV was used, equivalent to the spectrometer resolution. The same procedure was applied to Co L-edge emission reference spectra in order to check that no artefacts were introduced in the deconvolution.

The raw RIXS data are shown on a loss energy scale in Fig. 2a for several different incident photon energies between 777 eV (spectrum a) and 782 eV (spectrum g), spanning the Co L_3-edge absorption feature. The peak at 0 eV represents elastically scattered light. There are clear loss features present in all spectra below -4 eV, above which a weak and broad charge-transfer peak emerges centered about -6.7 eV. In order to accurately locate these peaks, a linear combination of Voigt functions was fitted to each spectrum, and the average center of each feature was determined. Altogether, three distinct loss features can be seen in the spectra: (i) at -0.83 eV clearly visible in spectra (d) and (f), (ii) at -2.08 eV in spectra (c-f), and at -3.37 eV in spectrum (d). These spectra, and the energies of these features, are similar to RIXS L-edge measurements of other Co^{2+} compounds, for example CoO[20].

The MaxEnt deconvoluted spectra are shown in Fig. 2b, and show obvious improvement in the linewidth of the features. In these spectra, the loss features previously identified are now much more clearly visible. For example, features (i) and (ii) are directly visible in all spectra, and (iii) is visible in all but the lowest energy spectrum (a). It is emphasized that no attempt to redetermine the energy location of these features with the new information provided by the MaxEnt algorithm has been made, yet they agree within ~ 0.1 eV in all spectra. It is noted that the noise level of the MaxEnt spectra is slightly higher than for the raw data, as might be

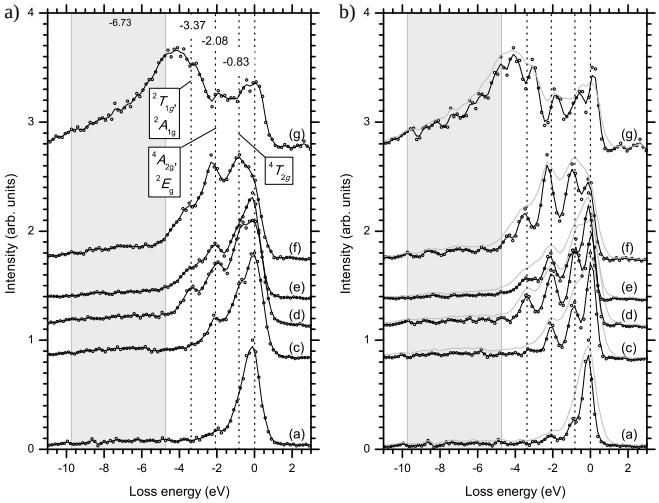

FIG. 2: Co L-edge RIXS data of $Co_3V_2O_8$. (a) Raw spectra, and (b) MaxEnt deconvoluted spectra, in which the raw spectra are reproduced in light grey. Solid lines are a guide to the eye and represent the data with a binomial smoothing of 0.15 eV. Vertical lines show the elastic line at 0 eV and loss features identified in the raw data. The symmetry of the excitations are labelled in (a).

expected in any deconvolution procedure. Nevertheless, focussing on features that persist across several incident photon energies allows one to be sure that the origin of a feature is intrinsic to the system under study, and not an artefact of the increased noise floor. The strength of this approach is anticipated to lie when spectral features are difficult to identify in raw data, as for example in spectrum (c), in which the -0.83 eV feature is hard to separate from the elastic peak.

IV. DECONVOLUTION OF ELASTIC PEAKS

As an additional test, the MaxEnt procedure has been applied to V L_3-edge RIXS data of $NdVO_3$ at room temperature, a system in which the occupation of the V $3d$ orbitals becomes ordered at low temperature[21]. Spectra were recorded with a spectrometer and incident photon resolution of 0.36 eV, yielding a total energy resolution of around 0.51 eV. Seven spectra were obtained approximately equally-spaced across the V L_3-edge absorption feature (and are shown in Fig. 3), and each spectrum was treated to the MaxEnt procedure with a broadening function of 0.36 eV. Again, the same procedure was applied to a Zn L-edge emission reference spectrum to ensure no artefacts were introduced in the deconvolution. The relative intensity of RIXS spectra at the V L-edge is weak, and so the spectra here have been summed together to yield 'averaged' loss spectra, shown in Fig. 3d for both the raw and MaxEnt deconvoluted spectra. The idea behind this procedure is that fluorescent features,

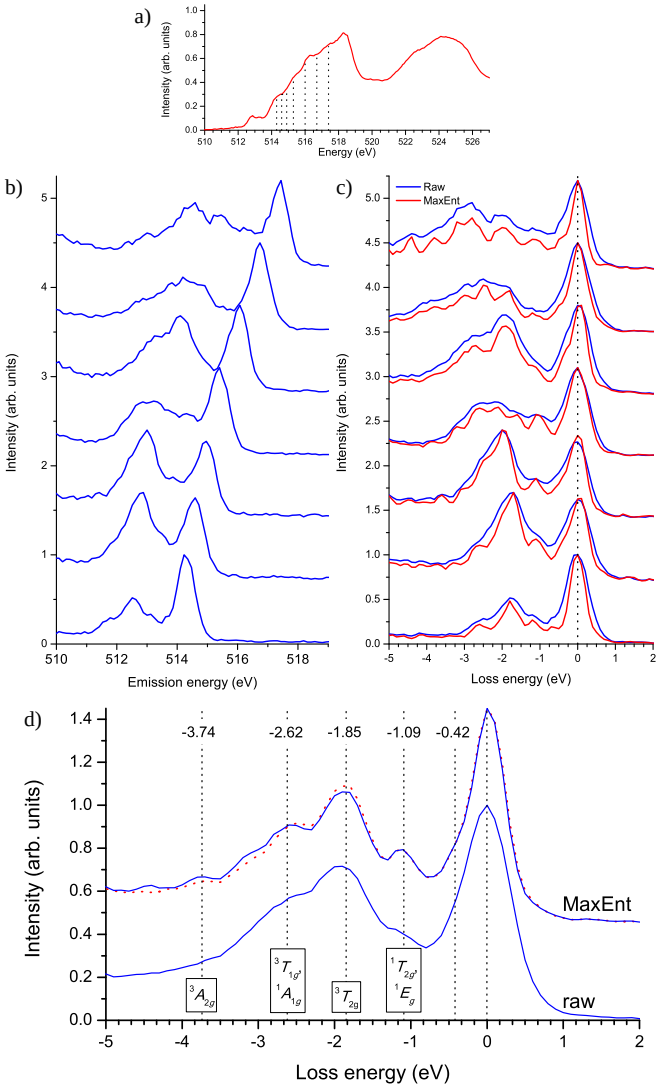

FIG. 3: (Color online) V L-edge RIXS data of $NdVO_3$. (a) The absorption spectrum and excitation energies used for RIXS. Raw RIXS data are shown on (b) an emission energy, and (c) a loss energy scale, for which the individual MaxEnt spectra are also shown. (d) Summed RIXS spectra before and after MaxEnt deconvolution. The symmetry of the excitations are labelled in (d); the dotted line represents the MaxEnt summed data with one spectrum missing (see text).

that are dispersive in loss energy, contribute a broad and weak background, whereas loss features will reinforce in the summed spectra. Note that there will be a slight additional broadening of the features due to uncertainty in the initial photon energy.

The individual raw spectra are shown in Fig. 3b. The first spectrum is on the onset of the V L_3-edge, in a location most suitable for exploring loss features. At higher excitation energies, V 3d fluorescence begins to contribute more strongly in the spectra, but is mostly concentrated beyond 2.5 eV from the elastic peak. Therefore, the subsequent interpretation of features in the summed spectra below this energy is less influenced by the presence of fluorescence. Moreover, the contributions from fluorescence do not reinforce across spectra, and provide a weak background to the summed spectra presented in the manuscript. In the raw summed spectra (Fig. 3d), two principle features are present: the elastic peak at O eV and a broader feature at around -2 eV. Shoulders either side of this second peak indicate the presence of other spectral features. Once the MaxEnt procedure is applied, however, the location of these weaker features becomes clear, at -2.62 eV and -1.09 eV either side of the -1.85 eV peak, and represent crystal field dd^* excitations. These features are also clearly identifiable in the individual deconvoluted spectra shown in Fig. 3c, particularly the lowest energy spectrum. Furthermore, however, a relatively weak shoulder is evident close to the elastic peak at -0.42 eV, and may represent an orbital excitation in the form of a bi-orbiton, previously observed for YVO_3 at 0.4 eV[22]. Its presence can also be inferred in the raw spectra from the slight asymmetry of the elastic peak in this spectrum. Finally, an additional feature at -3.74 eV, not visible in the raw spectrum, becomes clear after the MaxEnt deconvolution. This peak is harder to identify in the individual spectra, but is most prominant in the highest energy MaxEnt spectrum in Fig. 3c. In order to check its presence at more than one excitation energy (and ensure that its origin is not the fluorescent part of the spectrum), the highest energy MaxEnt spectrum has been removed from the summation in the dotted line of Fig. 3d, and indeed, this peak still persists. However, a higher energy feature (at around -4.5 eV) disappears in this process; although this may be a loss feature of the spectrum, further work is needed to confirm its origin.

The strong elastic peak in these data mean that we can directly measure the instrument resolution, since the elastic peak is a δ-function in the limit of an infinitessimally small total resolution function. In order to avoid complications with low-energy (e.g. phonon) excitations, all the following fits to the elastic peak have been constrained predominantly to its high-energy side. For the raw spectra, the FWHM of the elastic peak is 0.75 eV, slightly broader than expected, presumably in part due to the additional processing involved in summing these spectra (but possibly also due to some uncertainty in the slit width). For the MaxEnt spectra, however, the FWHM is 0.50 eV. Although at first glance this is not as narrow as one might expect, it should be remembered that this represents a combination of the incident photon resolution and the spectrometer resolution, and no attempt has been made to remove the incident photon resolution function. In this respect, the narrowing of the elastic peak behaves well, and corresponds to a narrowing of the 'effective' spectrometer resolution (by subtracting in quadrature the incident photon resolution, 0.36 eV, from the measured resolution) from 0.66 eV to 0.35 eV.

V. NOISE PROPAGATION

The propagation of noise through the MaxEnt procedure is a complex problem; indeed, with only a slightly different setup of the problem, MaxEnt can be used to 'de-noise' data or reconstruct missing information from sparse data[16,23]. In order to quantify the propagation of noise through the MaxEnt procedure, we have simulated a series (of $M = 100$) of noisy RIXS spectra, $P_i(E)$. These have then been passed through the MaxEnt deconvolution, and the variance in the resulting deconvoluted spectra analyzed,

$$\sigma^2[P(E)] = \frac{1}{M}\sum_{i=1}^{M}[P_i(E) - \bar{P}(E)]^2, \qquad (3)$$

where $\bar{P}(E)$ is the mean of the M simulated spectra. The test spectrum, $T(E)$, was chosen to approximate spectrum (d) in Fig. 2: a linear combination of Gaussian functions of 0.4 eV FWHM (similar to the beamline resolution used in the measurements) centered at 0 eV, -0.83 eV, -2.08 eV and -3.37 eV were added to a Gaussian function of 4 eV FWHM centered at -6.73 eV to approximate the elastic, dd^* and CT features respectively. This spectrum was then convoluted with a Gaussian function of 0.82 eV FWHM, approximating the spectrometer resolution, and scaled to contain 1000 counts in the peak data channel. The M simulated spectra were then created by adding randomly generated noise following a normal distribution with $\sigma(E) = \sqrt{T(E)}$, and are shown in Fig. 4a. These test spectra, $P_i(E)$, were each deconvoluted with the same parameters as used for the $Co_3V_2O_8$ data shown in Fig. 2.

The resulting deconvoluted spectra are shown in Fig. 4b. Comparison between the deconvoluted spectra and the initial test spectrum, $T(E)$ [shown by the dashed line in Fig. 4b], are very encouraging, and provide a direct visualization of the power of the MaxEnt algorithm. In order to ensure that the mean and variance are meaningful quantities, the inset shows the distribution of the data about the mean, in units of the standard deviation, for data between -9 and 1 eV (to restrict the contribution to the finite signal region of the spectra). Although there is a weak positive skewness in the distribution of the deconvoluted spectra (emphasizing the complexity of the MaxEnt noise problem), it is sufficiently close to a normal distribution that the mean and variance are still useful indicators of the distribution. This is important since it allows us to attach meaningful (statistical) errors to the deconvoluted spectra.

It is evident from Figs. 4a,b that, as expected, the noise level is slightly higher for the deconvoluted spectra (for example, compare the error bars for the peak at 0 eV in Fig. 4a and at -2 eV in Fig. 4b, for which the intensity is similar). For Poisson statistics, relevant in counting problems, the variance of a datum scales with its expected value (for $\bar{x} \gtrsim 10$), as shown in Fig. 4c in which the variance, σ^2, of the input data is plotted against its mean, $\bar{P}$. However, this is not the case for the deconvoluted

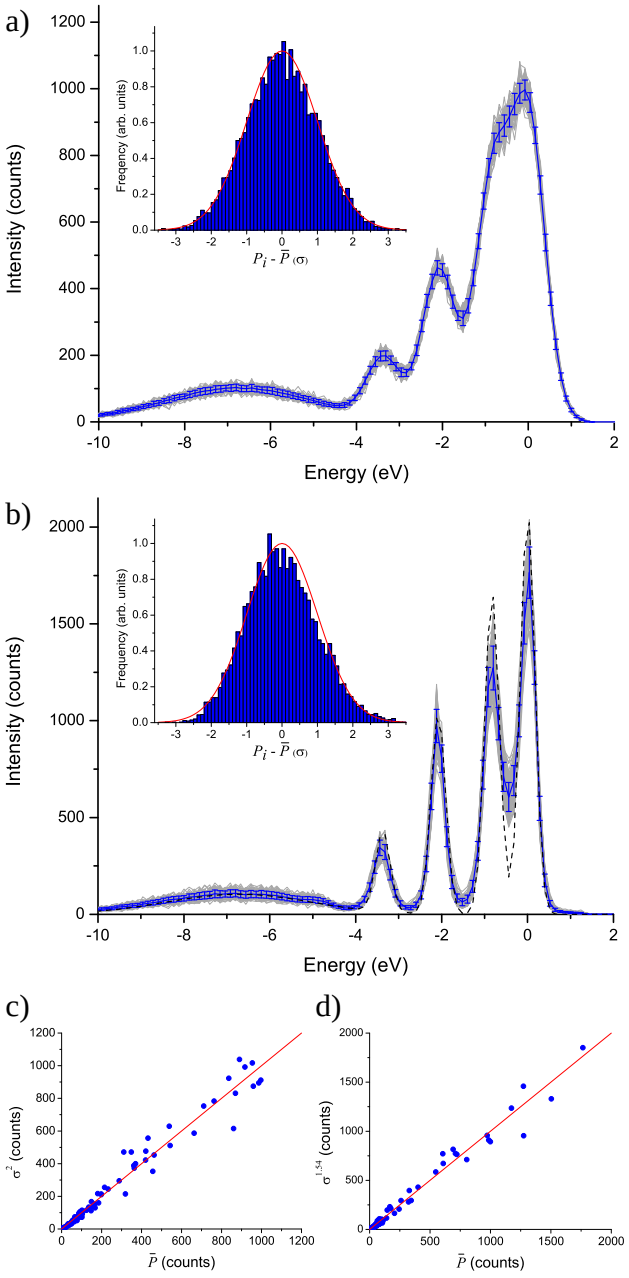

FIG. 4: (Color online) The results of deconvoluting $M = 100$ simulated noisy spectra with the MaxEnt procedure; (a) Input spectra, and (b) deconvoluted spectra. The individual spectra, $P_i(E)$, are shown in light gray, with the mean spectra, $\bar{P}(E)$, in blue. The error bars shown represent the standard deviation, $\sigma[P(E)]$, of the M spectra for each energy. The inset shows the distribution of each simulated spectrum from its mean, normalized to its standard deviation. In (b), the initial test spectrum, $T(E)$, is shown by the dashed line. (c) Comparison between the mean of the input spectra and their variance, σ^2. (d) Comparison between the mean of the deconvoluted spectra and $\sigma^{1.54}$. For (c) and (d) the solid line represents $\bar{P} = \sigma^2$ and $\bar{P} = \sigma^{1.54}$ respectively.

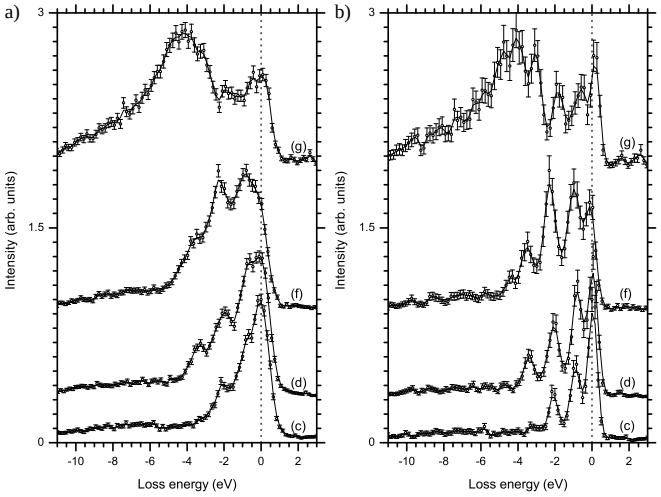

FIG. 5: (Color online) The (a) raw, and (b) MaxEnt deconvoluted RIXS spectra shown in Fig. 2, reproduced here with error bars. In (a), the statistical error is shown ($\sigma = \sqrt{N}$), whereas in (b) the empirical error $\sigma = N^{1/1.54}$ is used (see text).

spectra, indicating the propagation of errors through the MaxEnt process is non-linear with respect to the pixel intensity. Qualitatively, the relationship is super linear, meaning that pixels of high intensity (in the deconvoluted spectra) are more sensitive to statistical noise than those of lower intensity. Such behavior is connected with the tendency of the deconvolution to move counts from low intensity regions of the input spectrum towards higher intensity regions. Empirically, we find that the variance and mean are connected by $\bar{P} \sim \sigma^{1.54}$ for the range of $\bar{P}$ investigated here (approximately 50 – 2000), as shown in Fig. 4d, which corresponds to an approximate doubling of the noise ratio for a typical spectrum. It is emphasized that this analysis only reflects the propagation of statistical noise, and does not account for systematic errors that may be present in the process itself. The result of applying these empirical errors to the $Co_3V_2O_8$ RIXS data is shown in Fig. 5 for some representative spectra before and after the MaxEnt procedure. In each case, the visual scatter of the data points is consistent with the magnitude of the error bars, and the loss features that were previously identified are well above the noise level. Moreover, the apparent structure at high energies in the deconvoluted spectrum (g) is of the order of the noise, and is due to the poorer statistics recorded for this spectrum.

VI. CONCLUSIONS

In summary, the MaxEnt deconvolution procedure has been successfully applied to soft x-ray RIXS spectra. The deconvoluted spectra show a marked improvement in the resolution of spectral features without introduction of artefacts associated with the process or excessive increase in the noise ratio, allowing for greater confidence in separating and identifying loss features, such as crystal-field dd^* transitions or low-energy collective excitations. For example, a very recent application of MaxEnt has helped to clarify the RIXS features of $La_{1-x}Sr_xMnO_3$[24]. Detailed analysis of the propagation of noise through the MaxEnt procedure has been presented, and the noise ratio of deconvoluted spectra has been found to approximately double for the features of typical spectra. The process is quite general, and is not limited to the soft x-ray regime or 2D data, and is expected to perform equally well with, for example, x-ray absorption spectra or high-resolution RIXS. It is anticipated that the strength of the procedure is when spectral features are difficult to identify in raw data (but whose presence may already be inferred from that data, albeit indirectly).

Acknowledgements

The Boston University (BU) program is supported in part by the Department of Energy under Contract No. DE-FG02-98ER45680. The Advanced Light Source is supported by the Director, Office of Science, Office of Basic Energy Sciences, of the U.S. Department of Energy under Contract No. DE-AC02-05CH11231.

[1] A. Kotani and S. Shin, Rev. Mod. Phys. **73**, 203 (2001).
[2] L. J. P. Ament, M. van Veenendaal, T. P. Devereaux, J. P. Hill and J. van den Brink, Rev. Mod. Phys. **83**, 705 (2011).
[3] H. Liu, J.-H. Guo, Y. Yin, A. Augustsson, C. Dong, J. Nordgren, C. Chang, P. Alivisatos, G. Thornton, D. F. Ogletree, F. G. Requejo, F. de Groot and M. Salmeron, Nano Lett. **7**, 1919 (2007).
[4] J.-H. Guo, Y. Luo, A. Augustsson, S. Kashtanov, J.-E. Rubensson, D. K. Shuh, H. Ågren and J. Nordgren, Phys. Rev. Lett. **91**, 157401 (2003).
[5] F. Hennies, A. Pietzsch, M. Berglund, A. Föhlisch, T. Schmitt, V. Strocov, H. O. Karlsson, J. Andersson and J.-E. Rubensson, Phys. Rev. Lett. **104**, 193002 (2010).
[6] G. Ghiringhelli, A. Piazzalunga, X. Wang, A. Bendounan, H. Berger, F. Bottegoni, N. Christensen, C. Dallera, M. Grioni, J.-C. Grivel, M. Moretti Sala, L. Patthey, J. Schlappa, T. Schmitt, V. Strocov and L. Braicovich, Eur. Phys. J. Special Topics **169**, 199 (2009).
[7] J. Schlappa, T. Schmitt, F. Vernay, V. N. Strocov, V. Ilakovac, B. Thielemann, H. M. Rønnow, S. Vanishri, A. Piazzalunga, X. Wang, L. Braicovich, G. Ghiringhelli, C. Marin, J. Mesot, B. Delley and L. Patthey, Phys. Rev. Lett. **103**, 047401 (2009).
[8] L. Braicovich, L. J. P. Ament, V. Bisogni, F. Forte, C.

Aruta, G. Balestrino, N. B. Brookes, G. M. De Luca, P. G. Medaglia, F. Miletto Granozio, M. Radovic, M. Salluzzo, J. van den Brink, and G. Ghiringhelli, Phys. Rev. Lett. **102**, 167401 (2009).

[9] L. F. J. Piper, A. DeMasi, S. W. Cho, A. R. H. Preston, J. Laverock, K. E. Smith, K. G. West, J. W. Lu and S. A. Wolf, Phys. Rev. B **82**, 235103 (2010).

[10] L. Braicovich, G. Ghiringhelli, L. H. Tjeng, V. Bisogni, C. Dallera, A. Piazzalunga, W. Reichelt and N. B. Brookes, Phys. Rev. B **76**, 125105 (2007).

[11] L. Braicovich, J. van den Brink, V. Bisogni, M. Moretti Sala, L. J. P. Ament, N. B. Brookes, G. M. De Luca, M. Salluzzo, T. Schmitt, V. N. Strocov and G. Ghiringhelli, Phys. Rev. Lett. **104**, 077002 (2010).

[12] C. E. Shannon and W. Weaver, *The Mathematical Theory of Communication*, University of Illinois Press, (1949).

[13] S. F. Gull and J. Skilling, *Maximum Entropy and Bayesian Methods in Inverse Problems*, edited by C. R. Smith and W. T. Grandy, Dordrecht: Reidel (1985).

[14] S. B. Dugdale, M. A. Alam, H. M. Fretwell, M. Biasini and D. Wilson, J. Phys.: Condens. Matter **6**, L435 (1994).

[15] H. M. Fretwell, S. B. Dugdale, M. A. Alam, M. Biasini, L. Hoffmann and A. A. Manuel, Europhys. Lett. **32**, 771 (1995).

[16] S. F. Gull and J. Skilling, IEE Proc.-F **131**, 646 (1984).

[17] J. Nordgren, G. Bray, S. Cramm, R. Nyholm, J.-E. Rubensson and N. Wassdahl, Rev. Sci. Instrum. **60**, 1690 (1989).

[18] The second order emission features satisfy the second order of diffraction of the spectrometer diffraction grating, and therefore appear at half the energy of the first order emission features (Zn L_3 = 1011.7; Zn L_2 = 1034.7).

[19] G. Balakrishnan, O. A. Petrenko, M. R. Lees and D. McK. Paul, J. Phys.: Condens. Matter **16**, L347 (2004).

[20] S. G. Chiuzbăian, T. Schmitt, M. Matsubara, A. Kotani, G. Ghiringhelli, C. Dallera, A. Tagliaferri, L. Braicovich, V. Scagnoli, N. B. Brookes, U. Staub and L. Patthey, Phys. Rev. B **78**, 245102 (2008).

[21] S. Miyasaka, Y. Okimoto, M. Iwama and Y. Tokura, Phys. Rev. B **68**, 100406(R) (2003).

[22] E. Benckiser, R. Rückamp, T. Möller, T. Taetz, A. Möller, A. A. Nugroho, T. T. M. Palstra, G. S. Uhrig and M. Grüninger, New J. Phys. **10**, 053027 (2008).

[23] J. Skilling and S. F. Gull, Inst. Math. S. **20**, 341 (1991).

[24] L. F. J. Piper, J. Laverock, A. R. H. Preston, S. W. Cho, B. Chen, A. DeMasi, K. E. Smith, L. Saraf, T. Kaspar, J.-H. Guo and A. Rusydi, unpublished (2011).